JACS
JOURNAL OF THE AMERICAN CHEMICAL SOCIETY
pubs.acs.org/JACS
Article

Reduced Recombination and Capacitor-like Charge Buildup in an Organic Heterojunction

Kyra N. Schwarz, Paul B. Geraghty, Valerie D. Mitchell, Saeed-Uz-Zaman Khan, Oskar J. Sandberg, Nasim Zarrabi, Bryan Kudisch, Jegadesan Subbiah, Trevor A. Smith, Barry P. Rand, Ardalan Armin, Gregory D. Scholes,* David J. Jones, and Kenneth P. Ghiggino*

Cite This: https://dx.doi.org/10.1021/jacs.9b12526

Read Online

ACCESS | Metrics & More | Article Recommendations | Supporting Information

ABSTRACT: Organic photovoltaic (OPV) efficiencies continue to rise, raising their prospects for solar energy conversion. However, researchers have long considered how to suppress the loss of free carriers by recombination—poor diffusion and significant Coulombic attraction can cause electrons and holes to encounter each other at interfaces close to where they were photogenerated. Using femtosecond transient spectroscopies, we report the nanosecond grow-in of a large transient Stark effect, caused by nanoscale electric fields of ~487 kV/cm between photogenerated free carriers in the device active layer. We find that particular morphologies of the active layer lead to an energetic cascade for charge carriers, suppressing pathways to recombination, which is ~2000 times less than predicted by Langevin theory. This in turn leads to the buildup of electric charge in donor and acceptor domains—away from the interface—resistant to bimolecular recombination. Interestingly, this signal is only experimentally obvious in thick films due to the different scaling of electroabsorption and photoinduced absorption signals in transient absorption spectroscopy. Rather than inhibiting device performance, we show that devices up to 600 nm thick maintain efficiencies of >8% because domains can afford much higher carrier densities. These observations suggest that with particular nanoscale morphologies the bulk heterojunction can go beyond its established role in charge photogeneration and can act as a capacitor, where adjacent free charges are held away from the interface and can be protected from bimolecular recombination.

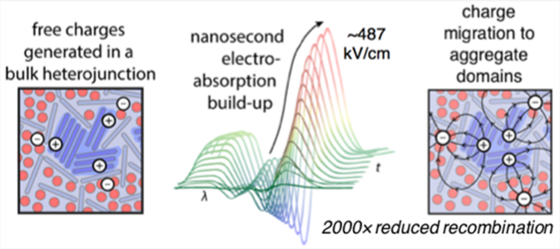

INTRODUCTION

One of the greatest challenges for light-harvesting technologies is the successful collection and usage of photogenerated charged species. The majority of organic photovoltaic (OPV) devices use a bulk heterojunction for their active layer—consisting of donor and acceptor domains—where molecular structural complexity is viewed as a challenge to be overcome for harvesting free carriers.[1,2] In contrast, photosynthetic light-harvesting complexes actually rely on nanoscale intricacies to create cascades that separate and hold mutually attracted charges at a distance for optimal quantum efficiency.[3]

The organic bulk heterojunction's nanoscale morphology is intimately involved in each stage of the energy conversion process. Following light absorption, excitons diffuse to a donor–acceptor interface where charges can be generated that in turn are transported to their respective electrodes in order to generate photocurrent and photovoltage.[4] In current high-performing OPVs, charge generation is fairly efficient and the recombination of separated charges can be considered the largest limitation of efficiency.[5,6] This is particularly important for scaling up organic solar cells to large areas using high-throughput fabrication systems.[7] Large-scale deposition demands junctions thicker than conventional active layers, i.e., larger than 100 nm. Due to low mobilities and significant bulk carrier recombination, organic solar cells often lose their efficiency in the thick junction limit. Only a few systems so far have shown promise in this regard, delivering high efficiencies even when the junction thickness exceeds 500 nm.[8−10] It has been demonstrated that the reason behind this is reduced recombination with respect to the Langevin encounter limit.[9,11] Among the few systems exhibiting reduced bimolecular recombination, the highest reduction factor (relative to the Langevin rate) so far has been 800 times.[8]

To understand the fate of photogenerated charges, we track their time-resolved photoinduced absorption and also examine the influence of local electric fields formed by charge carriers that can be detected by the use of an electroabsorption or Stark signal.[12] This effect occurs when an electric field perturbs an optical transition, which is sensitive to either its change in dipole or change in polarizability in the presence of the field. This

Received: November 20, 2019
Published: January 10, 2020

signature can be observed when a macroscopic electric field is applied to a light-absorbing species, as in Stark spectroscopy.[12−15] It can also be caused directly by photogenerated charges, where it has been used as a probe of charge separation at the nanoscale,[16−18] including for subpicosecond charge transfer in bulk heterojunctions.[19−22]

In this work, we demonstrate that the bulk heterojunction morphology can play an unforeseen role, keeping adjacent free carriers apart via capacitive charging. An active layer morphology consisting of pure and intermixed domains is able to block a key recombination pathway to triplet excitons and suppress bimolecular recombination up to 2000 times greater than that predicted by the Langevin model. This is the largest reduction factor so far reported in a technologically relevant organic solar cell. This occurs concurrently with large electric fields that build up following charge generation in these systems and are maintained across domains for nanoseconds, resembling the charging of a capacitor. To our knowledge, this interdomain capacitive effect, manifested by a local electric field buildup with a magnitude of ∼487 kV/cm, is unprecedented in any photovoltaic system. The dielectric constant of the material dictates that the dielectric polarization of intervening amorphous and interfacial domains in the presence of such fields must further protect charges, much like the dielectric layer in a macroscopic capacitor. Rather than being detrimental, we show that this electric field buildup is related to the prevention of nonradiative loss pathways and substantial improvements in device performance, including in thick junction devices.

■ EXPERIMENTAL SECTION

Sample and Device Preparation. BQR was prepared according to a synthetic procedure published previously.[23] To prepare neat films, BQR and $PC_{71}BM$ (Nano-c, 99%) were first dissolved in chloroform (HPLC grade) to a concentration of 10 mg/mL. To prepare blend films, solutions of BQR and $PC_{71}BM$ were prepared by dissolving, respectively, in chloroform to a concentration of 13.3 mg/mL (95 nm "thin" films), 16.5 mg/mL (110 nm films), 20 mg/mL (140 nm "thick" films), and 32 mg/mL (220 nm films) and then combining in equal parts for 1:1 blends w/w and a ratio of 95:5 for majority BQR active layers. The substrates were cleaned by sonicating sequentially in 1 M NaOH, distilled water, acetone, isopropanol, and dichloromethane, followed by 15 min of UV/ozone treatment. All films were cast onto clean glass substrates via spin coating at 1000 rpm (2000 acceleration) for 30 s. Solvent vapor annealing was conducted in a tetrahydrofuran (THF) atmosphere with an exposure time of 20 s.

Organic photovoltaic devices were processed on prepatterned indium tin oxide (ITO)-coated glass substrates with a sheet resistance of 15 Ω/sq. The conventional devices were fabricated with a device geometry of glass/ITO/PEDOT:PSS/active layer/Ca/Al. The ITO-coated glass substrates were cleaned by ultrasonic treatment in acetone and isopropyl alcohol for 15 min each and subsequently treated in UV−Ozone for 15 min. A thin layer (30 nm) of PEDOT:PSS (Clevios P VP AI 4083, filtered at 0.45 μm) was spin coated onto the ITO surface. After baking at 150 °C for 10 min, the substrates were transferred into a nitrogen-filled glovebox. Subsequently, the active layer was spin coated from blend chloroform solutions with a weight ratio of donor and $PC_{71}BM$ at 1:1. Then the substrates were suspended over a glass Petri dish containing 1 mL of THF for solvent vapor annealing (SVA). After SVA treatment, the films were transferred to a metal evaporation chamber, and a bilayer cathode consisting of Ca (30 nm) capped with Al (100 nm) was deposited through a shadow mask (active area was 0.1 cm^2) at approximately 1×10^{-6} Torr.

Steady-State Spectroscopy. Absorption spectra of all films were recorded using a Varian Cary 50 UV−Vis spectrophotometer. Fluorescence spectra were recorded on a Varian Eclipse spectrofluorimeter using an excitation wavelength of 600 nm, where all spectra were corrected. The optical constants were obtained through spectroscopic ellipsometry using a J.A Woollam Co. M-2000 ellipsometer.

Electrical Charge Transport and Recombination Measurements. Resistance dependent photovoltage (RPV) measurements were conducted using a Pharos PH1-10 laser at the second harmonic wavelength of 514 nm. The pulse duration was approximately 290 fs, and the fluence was lowered to less than 1 nJ/cm^2 using neutral density filters. The repetition rate of the experiment was 20 Hz. The device was mounted in a closed metal box acting as a Faraday cage to minimize the pick-up noise. The transients were recorded using a Rohde&Schwartz RTM3004 oscilloscope. A homemade decade variable-resistance box was used to vary the series resistance of the circuit from 50 Ohms to 1 MOhms. The transient double-injection measurements were done using the same oscilloscope, and a Keysight 33500B function generator was used to apply the voltage pulse to the devices in forward bias. Steady-state currents were recorded using a Keithley 2450 source-meter unit.

Electro-optical Device Simulations. For the device simulations, a numerical steady-state drift-diffusion model was used.[24] The device model solves the drift-diffusion current equations in conjunction with the charge carrier continuity equations and the Poisson equation for a given applied voltage and charge carrier generation rate at AM1.5G incident light intensity. The recombination rate between charge carriers was taken to be bimolecular with a recombination coefficient reduced by a factor of γ compared to Langevin recombination. Furthermore, the carrier densities at the contacts are assumed to be in thermal equilibrium. The parameters used are listed in the Supporting Information. The generation rate was calculated based on the optical constants of the device stack using a transfer matrix model that takes into account the back-electrode reflection and interference effects of the optical electric field inside the device.[25]

Transient Absorption Spectroscopy. Transient absorption spectroscopy was undertaken on a 92 kHz repetition-rate laser and reproduced on a 1 kHz system, both of which are described here.

For the high repetition rate system, a mode-locked Ti:sapphire oscillator (Coherent, Mira Seed) seeded a Ti:sapphire regenerative amplifier system (Coherent, RegA 9050) to produce pulses of ∼50 fs duration at a repetition rate of 92 kHz and a wavelength centered at 800 nm. The 600 and 553 nm pump beams were generated with an optical parametric amplifier (OPA9450, Coherent). The pump beam was mechanically chopped at ∼3.5 kHz, and the arrival time of the pump pulses relative to the probe was manipulated using a variable optical delay line (Newport, UTS150PP with ESP 300 controller). The broadband probe was derived from the residual 800 nm beam focused onto a 3 mm sapphire substrate (Crystal Systems) for measurements in the visible region (450−800 nm) and a 5 mm undoped YAG substrate (Crystal Systems) for the infrared region (800−1400 nm). After passing through the sample, the probe beam was analyzed with a CMOS detector (Ultrafast Systems) at ∼7077 spectra/s, and the excess 800 nm laser fundamental was removed using low- and high-pass filters for the visible and IR regions, respectively. For all measurements, unless otherwise noted, the pump beam was attenuated to a pulse power of 3.2 nJ/pulse with a spot area of 1.3×10^{-3} cm^2, giving a pump power density of 2.5 μJ/cm^2. Nitrogen was blown over films for all measurements. For further details on this experimental setup, see ref 26.

Ultrafast TA measurements were additionally conducted and replicated with a 1 kHz Ti:sapphire regenerative amplifier system (Coherent Libra) with an output of 800 nm pulses with ∼45 fs pulsewidth and approximately 4 W power. The pump arm of the Libra output was directed to an optical parametric amplifier (Light Conversion OPerA) and thereby converted into 600 nm pulses. The probe arm of the Libra output was directed to a commercial transient absorption spectrometer (Ultrafast System, Helios) and used in the generation of a visible and NIR continua from ∼450 to 800 nm and from 800 to 1500 nm, respectively. Optical filters were incorporated in order to separate out excess 800 nm remaining from the continua generation. Referencing of the probe spectra using a second camera was required to achieve adequate signal-to-noise at low pump fluence. The pump beam spot size was measured by analyzing the image obtained by a digital CCD camera (Thorlabs Inc.) with Thorcam Software (Thorlabs Inc.) placed at the pump probe overlap. The size of the pump beam at ca. 600 nm was approximately 3.8×10^{-3} cm^2. The pump power was measured with a high-sensitivity optical power sensor (Coherent, Santa Clara, CA). Incident pump power in the visible region was ~9.5 nJ per pulse, giving a pump fluence of 2.5 μJ/cm^2.

Transient absorption experiments with a time delay of >10 ns were carried out using Helios-EOS (Ultrafast Systems), where the pump beam was used as described above. Probe pulses (~2 ns duration) were generated by a built-in photonic crystal fiber-based supercontinuum pulsed light source with an electronic delay between the pump and the probe.

For both measurements, unless otherwise indicated, an excitation density of 2.5 μJ/cm^2 was used to prevent artifacts associated with exciton−exciton[27] and exciton−charge annihilation.[28,29] The relative orientation of pump and probe polarization was 54.7° (magic angle), and all spectra were corrected for the chirp of the supercontinuum probe.

Grazing Incidence Wide-Angle X-ray Spectroscopy (GIWAXS). GIWAXS measurements were conducted at the SAXS/WAXS beamline of the Australian synchrotron. The substrates were silicon wafers that had been sonicated in acetone and isopropanol for 30 min each followed by 15 min of UV/ozone treatment. The measurements were performed with an X-ray energy of 11 keV and a range of incident angles from $\Omega = 0.025$ to 0.5 in 0.01−0.05 increments to allow signal optimization near the critical angle of the polymer film but below the critical angle of the substrate. Data from GIWAXS experiments were analyzed using a customized version of NIKA 2D based in IgorPro.

Steady-State Electroabsorption Measurements. Electroabsorption (EA) samples were fabricated on prepatterned indium tin oxide (ITO) substrates by spin coating a BQR:PC$_{71}$BM (1:1) solution. A 10 mg/mL stock solution was made in chloroform. Spin coating was conducted in N_2 glovebox at 1000 rpm for 30 s and annealed at 100 °C for 10 min. Later, 10 nm of bathocuproine (BCP) was vacuum evaporated on the BQR:PC$_{71}$BM film, followed by 100 nm of aluminum (Al). Profilometer measurements of the films gave a thickness of 73.6 nm for the active layer, giving a total of 83.6 nm thickness between electrodes.

EA measurements were conducted in reflection mode, with the light beam reflecting off the back Al contact of the EA sample, passing the active layer twice. The direct reflected light was collected using a Si photodetector. The sample was biased with −1 V dc to prevent charge injection. A 1 kHz ac modulating voltage of amplitudes 0−5 V, at an interval of 200 mV was applied, superimposed on the dc voltage. The difference in reflection from the sample with applied ac voltage was measured using a lock-in amplifier, detecting the second-harmonic signal, 2δ, from the photodetector.

Computational Methods. Density functional theory (DFT) calculations were performed using Gaussian 16.[30] Geometry optimization and calculation of the dipole moment and polarizability was performed using the 6-31G(d,p) basis set and the B3LYP functional.

RESULTS AND DISCUSSION

We report studies of thin films of the electron donor BQR (benzodithiophene−quaterthiophene−rhodanine)[23] (Figure 1a) and blends with an electron acceptor PC$_{71}$BM ([6,6]-phenyl-C$_{71}$ butyric acid methyl ester). Neat BQR films consist of both amorphous and aggregate species, where π-stacked molecules can be identified by their vibronic structure on the low-energy end of the absorption spectrum (580−700 nm) (Figure 1b). This aggregation is somewhat interrupted when incorporated into a film with PC$_{71}$BM (Figure 1b, bottom).

These films undergo a dramatic change in photovoltaic power conversion efficiency (PCE) as a result of subtle changes to film morphology, which is controlled by processing. As-cast 1:1 BQR:PC$_{71}$BM bulk heterojunction devices (140 nm thick) have PCEs of 4.2%, increasing to 9.6% after a brief THF solvent vapor annealing (SVA) treatment[5] (Figure 2a and Figure S1). During the SVA process, the active layer swells with THF molecules, allowing BQR domains to undergo Ostwald ripening and form small but pure aggregates in the blend. This aggregation leads to the recovery of vibronic structure seen in Figure 1b (green lines) and an increased (010) reflection in X-ray scattering data (see Figure S2−S3), both indicating π−π stacking. The quenching of BQR exciton emission with blend film formation (see Figure S4) gives ~93% quenching for as-cast films compared to 79% for SVA, indicating that with annealing BQR domains increase in size and purity.

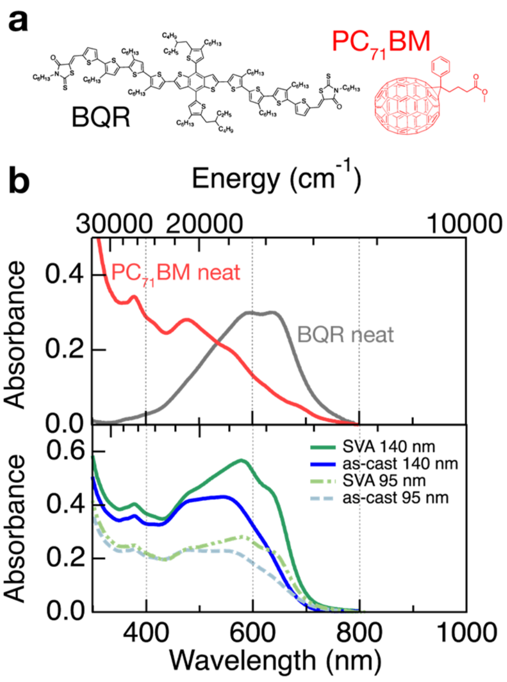

Figure 1. (a) Chemical structures of BQR and PC$_{71}$BM. (b) Absorbance of neat donor BQR and neat acceptor PC$_{71}$BM films (top) and 1:1 BQR:PC$_{71}$BM blend films (bottom) with a ~140 nm thick active layer; as-cast (blue solid) and SVA (green solid). Thinner blend films with a ~95 nm thick active layer are shown in dashed lines: as-cast (blue dashed) and SVA (green dashed).

The drastic increase in device performance upon changes in morphology becomes particularly apparent for thicker junctions. For active layers with a thickness of 320 nm (Figure 2a), the as-cast device displays a relatively poor PCE of 3.45% and fill factor (FF) of 41.4%, whereas the SVA device shows a PCE of 9.75% and a FF of 74.3%, exceptionally high for a 320 nm thick junction. A high PCE of 8.14% is maintained for 600 nm thick SVA devices (see Figure S5) exhibiting an unprecedented FF at these thicknesses of 60.7%. Resistance-dependent photovoltage measurements on the as-cast device (Figure 2b) reveal imbalanced mobilities of 1.5×10^{-3} and 4×10^{-5} cm^2/(V s) assigned to electrons and holes, respectively. Furthermore, double-injection (DoI) current transient measurements (Figure 2c) on the as-cast device suggest a Langevin reduction factor of $\gamma \approx 10$. These findings are fortified by electro-optical device simulations (Figure 2a) which reproduce the measured J−V characteristics using the extracted transport parameters and complex refractive indices as input. Importantly, the simulations suggest that (electric-field-dependent) geminate recombination is negligible under solar cell operating conditions.

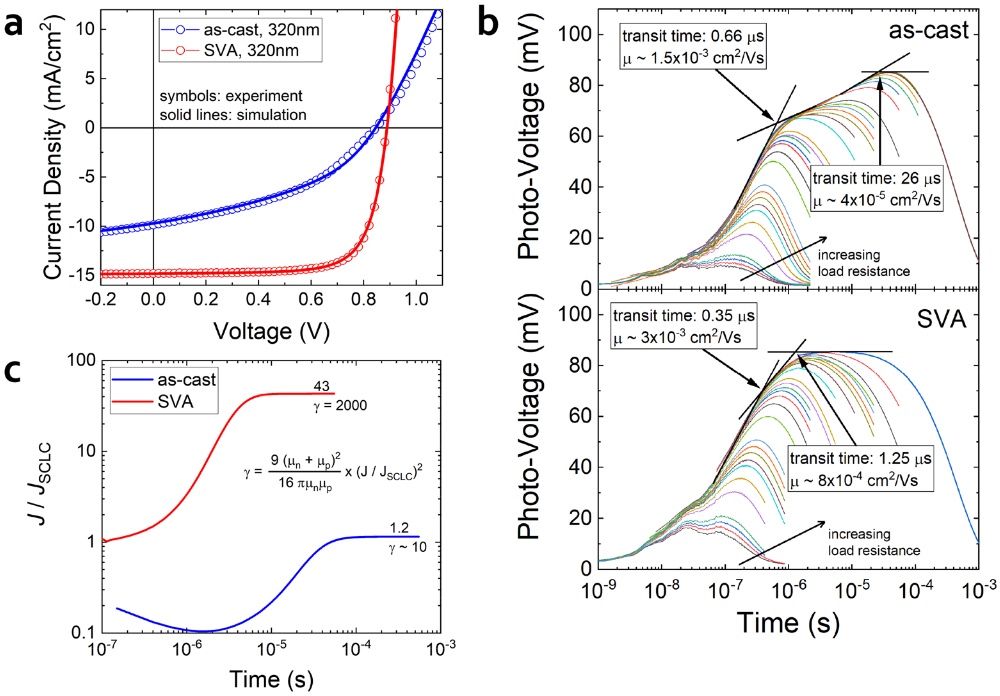

Figure 2. (a) Experimental $J-V$ curves of 320 nm thick as cast (blue circles) with PCE = 3.45% and FF = 41.4% and SVA device (red circles) with PCE = 9.75% and FF = 74.4%. Simulated $J-V$ curves using the electro-optical device model are indicated by the corresponding solid lines. (b) Resistance-dependent photovoltage transients for the as-cast (upper) and SVA (lower) device. Extracted transit times with the associated mobilities (μ) are indicated. (c) Double-injection current transient measurements on as-cast (blue) and SVA devices (red) for determination of the Langevin recombination reduction factor γ. Currents have been normalized to the corresponding space-charge-limited current $J_{\mathrm{SCLC}} = 9\varepsilon\varepsilon_0\,(\mu_n + \mu_p)\,(V - V_{bi})^2/8d^3$, where V is the applied voltage and ε is the vacuum permittivity (meaning of the other parameters is given in Table S2).

The SVA device, in turn, exhibits fairly balanced mobilities (Figure 2b) with a hole mobility of 8×10^{-4} cm^2/(V s) and an electron mobility of 3×10^{-3} cm^2/(V s). The increased hole mobility is consistent with larger and more pure BQR domains, expected upon SVA. Improved electron mobility (approaching that of neat $PC_{71}BM$) indicates better percolation between the $PC_{71}BM$ domains. DoI measurements on the SVA devices (Figure 2c) reveal a heavily suppressed Langevin reduction factor of $\gamma = 2000$. This reduction factor is the largest ever reported in a technologically relevant and efficient system. These results are corroborated by electro-optical device simulations (Figure 2a) assuming negligible geminate recombination.

The drastically increased device performance upon SVA can thus be attributed to a significantly reduced recombination coefficient. While the measurements on as-cast devices can be explained by a recombination coefficient based on diffusion-controlled encounter of electrons and holes that are initially in separate phases,[31] the impressive reduction of the recombination coefficient upon SVA cannot be explained based on charge carrier encounter in a simple two-component (donor:acceptor) system alone. Strong suppression of bimolecular recombination has been previously assigned to the fast dissociation of charge transfer states relative to the decay rate of the singlet CT states as well as back electron transfer of the triplet CT states.[32−34]

To understand the fate of photogenerated charges, we probe their photoinduced absorption and also track their evolution using a striking and slowly increasing Stark signature that is evident in transient data for the solvent vapor-annealed films. In ultrafast transient absorption measurements, blend films were photoexcited at 600 nm in order to preferentially create excitons in the BQR donor. Figure 3a−d shows femtosecond transient spectra of BQR:$PC_{71}BM$ blend films. As-cast films of 140 nm thickness (Figure 3a) are compared to films having undergone SVA treatment: a 95 nm "thin" film (Figure 3b) and a 140 nm thicker film (Figure 3c). The BQR exciton photoinduced absorption (PIA) signature was identified from measurements on neat BQR films (Figure S6a and Figure 3d), which can clearly be observed in all blend film transient spectra centered around 1100 nm with a lifetime of 160 ps. A second PIA can also be observed in all three spectra from 700 to 950 nm, corresponding to the BQR hole polaron as the result of charge transfer in the donor−acceptor blend. This hole polaron band allows us to detect the generation of charges. Temporal slices of the BQR hole polaron region at 920 nm (Figure 3e) reveal that charge transfer occurs predominately within the 200 fs instrument response time in all blend films despite differences in film crystallinity. As Samuel et al. have shown in their work on exciton diffusion in this system, the increase in domain size is accompanied by an increase in exciton diffusion rate; therefore, charge generation remains efficient even for large domains.[35] The as-cast film (Figure 3a) also contains a further photoinduced absorption at 1100 nm assigned to the BQR triplet species, which is discussed below.

In our transient absorption data, a strong electroabsorption signal (without any applied external field) is identified by its derivative-like signature around the BQR band edge (620−720 nm) and is most pronounced in the 140 nm thick SVA sample (Figure 3c and Figure 3i). This Stark shift is caused by the field established due to charges that are intrinsically photogenerated in the active layer rather than by any electrodes or external electric field. The chromophores affected by the electric field are overwhelmingly unexcited ground state molecules (rather than excited state molecules), due to the low excitation densities used and high probability that they will be in the vicinity of any fields

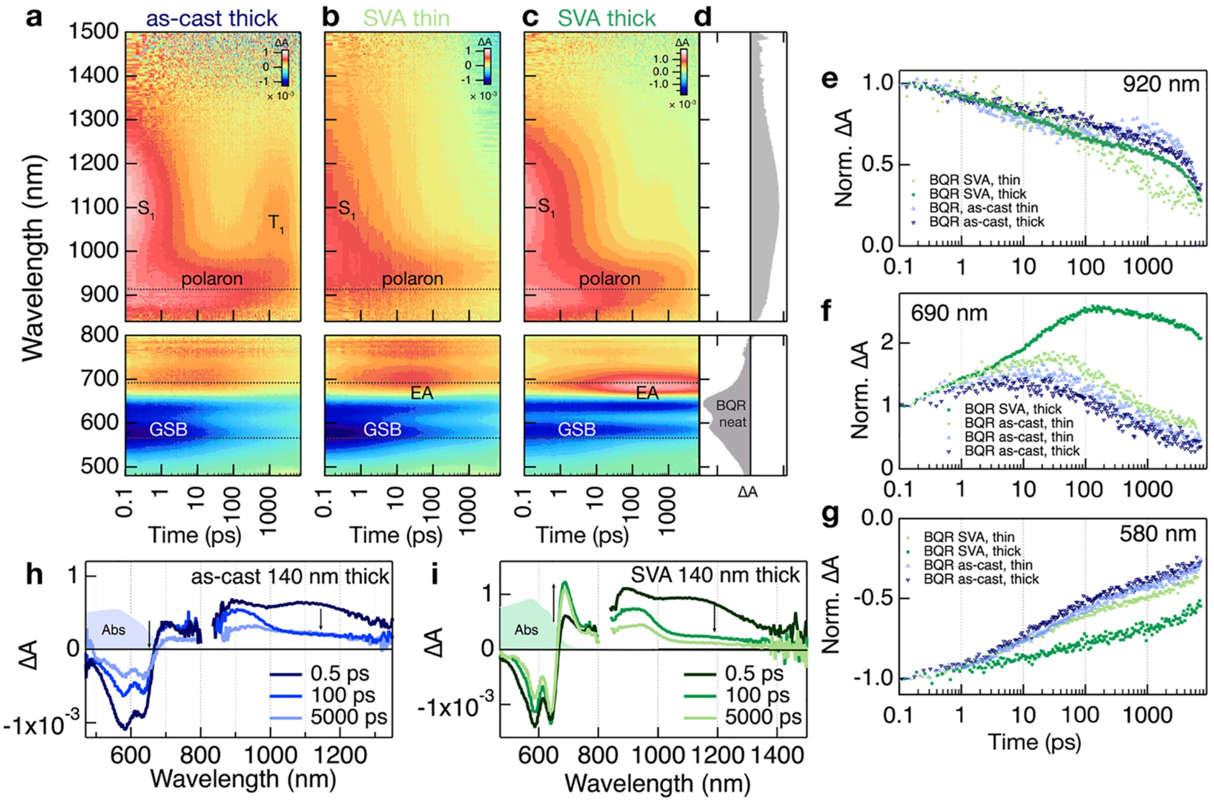

Figure 3. Results of ultrafast spectroscopy experiments: (a) 140 nm thick BQR:PC$_{71}$BM blend films as cast, (b) 95 nm thick BQR:PC$_{71}$BM blend films after SVA, and (c) 140 nm thick BQR:PC$_{71}$BM blend films after SVA. (d) Transient spectra of the BQR exciton for comparison. Dominant species are labeled as "GSB" (ground state bleach), "EA" (electroabsorption), "polaron" the BQR hole polaron, "S$_1$" the BQR exciton, and "T$_1$" the BQR triplet species. Normalized kinetics at different wavelengths: (e) 920 nm (polaron PIA), (f) 690 nm (electroabsorption), and (g) 580 nm (ground state bleach). Spectral slices are shown for (h) the "thick" 140 nm as-cast blend film and (i) the "thick"140 nm SVA blend film.

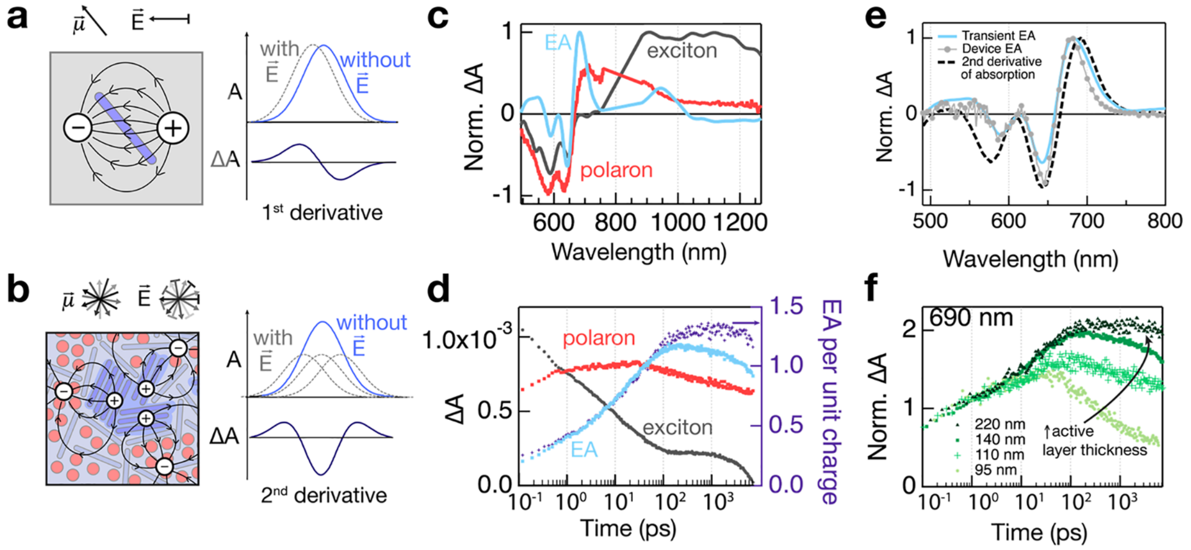

Figure 4. Electroabsorption signature. (a) Electroabsorption effect from an orientated chromophore where the transition dipole moment, $\Delta\vec{\mu}$, in an electric field, $\vec{E}$, results in a shift of the absorption spectrum, where the difference or Stark spectrum has a first-derivative line shape. (b) When the electric field and chromophores are at a range of relative orientations, the difference spectrum appears as the second derivative of the ground-state absorption. (c) Extracted transient spectra from 140 nm SVA films, comprising an exciton (black), polaron (red), and EA signal (blue), with their dynamics shown in d. (e) Extracted EA from the SVA blend film, steady-state device EA, and second derivative of the SVA BQR:PC$_{71}$BM ground state absorption spectrum. Extracted electroabsorption kinetic is divided by the polaron signal in d to give the magnitude of the EA contribution to the transient absorption per unit charge (right axis). (f) Increase in electroabsorption signal (at 690 nm) for SVA BQR:PC$_{71}$BM active layers with identical processing but of increasing thickness.

formed. The normalized kinetics at 690 nm show a rise over ~100 ps accompanied by a preserved ground state bleach intensity (580 nm) (Figure 3f–g). While the EA grow in is striking in the thicker solvent vapor-annealed film (Figure 3i),

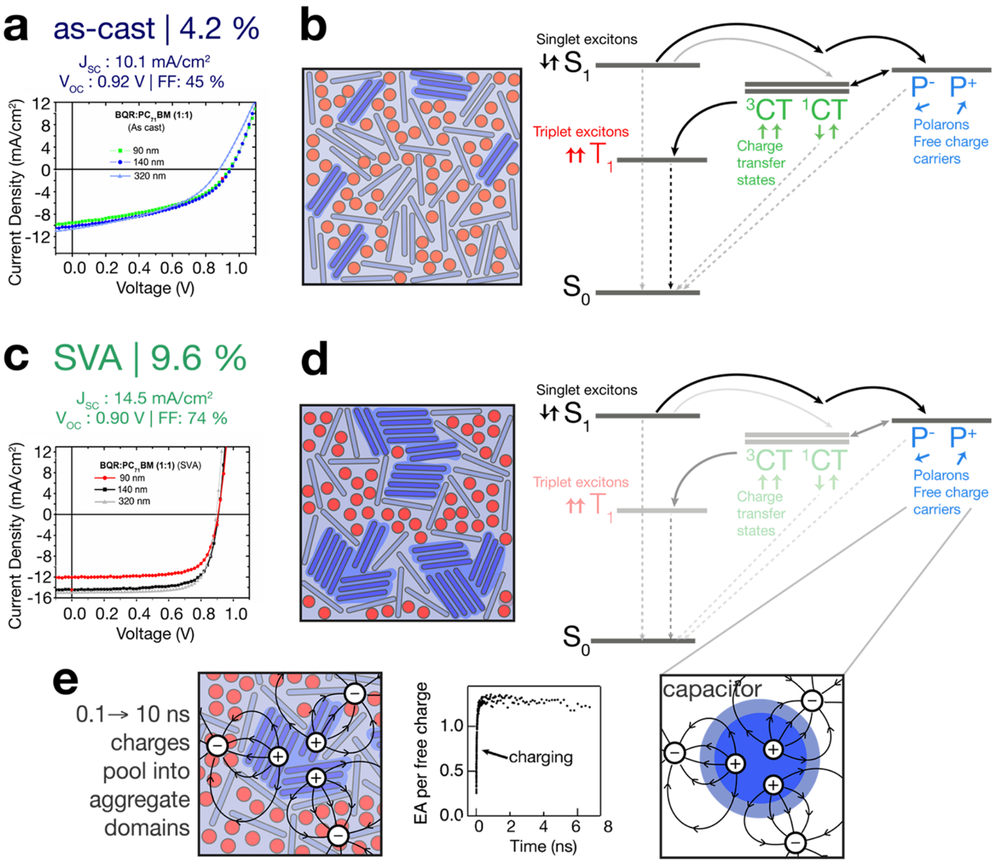

Figure 5. Fate of charge carriers (a) *J*−*V* curves and efficiencies for as-cast BQR:PC$_{71}$BM blend (140 nm thick). (b) Schematic of the morphology and dominant charge generation pathways. (c) *J*−*V* curves and efficiencies for solvent vapor-annealed BQR:PC$_{71}$BM blend (140 nm thick). (d) Schematic of the morphology and the dominant charge generation pathway, where a strong electroabsorption buildup is present. (e) Aggregate domain charge pooling that causes the EA signature to build and then be maintained over nanosecond time scales and its resemblance to charge buildup in a capacitor.

the feature is limited in other samples (Figure 3a and 3h and Figure S7) and is far less pronounced in thinner 95 nm SVA films (see Figure 3b).

For a Stark effect affecting a change of polarizability of a transition, interaction with an electric field will induce a dipole moment only in the direction of the field, regardless of the molecule's orientation, resulting in a first-derivative line shape of the EA signal.[13] In contrast, a change in dipole moment can result in either a first- or a second-derivative signal depending on orientational effects. A well-defined relative orientation between a transition dipole moment of a chromphore, $\Delta\mu$, and an electric field would lead to a unidirectional shift of the ground state absorption and consequently a change in absorption with a first-derivative line shape (Figure 4a) (see also Supporting Information section S4).[20]

Alternatively, a variety of orientations between many transition dipole moments, $\Delta\mu$, and electric field lines results in transition shifts to a range of both higher and lower energies, in other words the band broadens (Figure 4b), resulting in a difference spectrum with a line shape that is the second derivative of the ground state absorption.[12,13] When an external electric field is applied across a BQR:PC$_{71}$BM bulk heterojunction device, a clear second-derivative electroabsorption signal from the BQR component is observed in the steady-state absorption with increasing applied voltage (Figure S10a and device EA in Figure 4e).

By fitting this steady-state EA, BQR has a transition dipole moment, $\Delta\vec{\mu}$, of 8.43 D, typical for a Frenkel exciton, and a small change in polarizability, $\Delta\alpha$, of 35.38 Å^3. This indicates that the BQR transition dipole rather than the polarizability change is predominantly responsible for the Stark response of the material, hence, the dominant second-derivative spectral shape (see Figure S10 and S11). The ground state dipole is not expected to have a significant impact in this system; from DFT calculations (see Figure S12) BQR has a very small ground state dipole moment, $\vec{\mu}$, of 1.16×10^{-4} Debye and a ground state polarizability, α, of 315.33 Å^3.

To monitor the EA signature directly, the 3D transient surface was decomposed into its principal spectra and kinetics (Figure 4c and 4d) via global analysis based on a genetic algorithm,[20] where the neat BQR exciton and polaron spectra were used in the fitting procedure (see Supporting Information, section S5 and Figure S13). The data can be well-described by three components, the extracted kinetics showing that excitons form hole polarons either within the instrument response time or soon after. The electroabsorption component resembles the second derivative of the ground state SVA BQR:PC$_{71}$BM absorption spectrum and very closely resembles the steady-state electroabsorption of BQR excitons in a device with applied macroscopic electric field (Figure 4e and Figure S10). The EA signal intensity increases from almost zero over hundreds of picoseconds, while concurrently the polaron signal is maintained (Figure 4d).

The signal is caused by electrons and holes generated within the film, where the electric fields between these carriers perturb the ground state optical absorption of surrounding chromo-

https://dx.doi.org/10.1021/jacs.9b12526

phores. Interestingly, and in contrast to the dynamics of other species in the transient absorption data, the EA dynamics are significantly dependent on device thickness (Figure 4f and Figure S14), which is discussed further below. The EA dynamics are also very sensitive to pump power (Figure S9a), down to ~5 μJ/cm^2, which along with their pico- to nanosecond dynamics indicates that they are caused by free charge carriers. A second-derivative line shape also infers that the signal corresponds to a population of many dipole orientations relative to that of the electric fields[12] (Figure 4b). The EA signal shown here contrasts with previous reports in the literature in that here the migration of free carriers is responsible for this Stark effect rather than fast initial charge separation. Previous reports show intrinsic electroabsorption effects in organic bulk heterojunctions on much shorter time scales, decaying immediately after photoexcitation due to the initial charge separation events at an interface.[19−22,36] In a variety of systems these signals manifest as first-derivative Stark signals and persist and then decay on the time scales of charge separation, generally 100 fs or, in rare cases, a few picoseconds.[21] The conventional wisdom on this topic describes an electric field between charges decaying as carriers diffuse away from one another.[37] However, we see the opposite with a field increasing in magnitude up to 1 ns as a capacitive build-up occurs. After this time the magnitude of the EA signal is maintained on the time scale of >1 ns, though longer time transient data reveal that it does not remain on the time scale > 100 ns (Figure S8), suggesting that it would not act as a terminal trap for charge carriers.

An interesting control is provided by BQR:PC$_{71}$BM active layers that are not solvent vapor annealed; we do not observe any electric field buildup in as-cast BQR:PC$_{71}$BM active layers. Rather, polarons are lost via recombination of free charges to BQR triplet excitons.[33,38,39] The formation of triplets occurs on the same time scale as the polaron decay and can be seen as a photoinduced absorption in Figure 3a, centered at 1050 nm and appearing ~200 ps after excitation (further details are provided in Figure S15). The formation of this species is analogous to the recombination of injected charges in an LED, where spin-uncorrelated free charges recombine at a 3:1 ratio of triplet:singlet charge transfer states (Figure 5a and 5b).

We do not see any evidence that geminate recombination contributes as a significant decay pathway in the as-cast films. First, the polaron signal and triplet signal of as-cast films are power dependent (Figures S9b and S15b, respectively), indicating that bimolecular recombination dominates here. Second, by comparing the ground state bleaches (Figure 3g), the 90 nm (thinner) as-cast and SVA samples have very similar bleach recovery dynamics. The device performance is very different, but with similar bleaches, geminate recombination to the ground state does not appear to be a major contributor. When comparing the thicker 140 nm films, the SVA film has a significant EA contribution to its bleach (Figure 3c), making it more difficult to compare this dynamic. Finally, $J-V$ simulations (Figure 2a) give an excellent match to experiment and suggest that (electric-field dependent) geminate recombination is negligible under solar cell operating conditions.

The distinctive pathways for free charges shown here are reflected in devices made from these active layers. As-cast devices (140 nm thick), with the bimolecular loss pathway to the triplet exciton, have efficiencies of ~4.2% (Figure 5a and 5b) with an open-circuit voltage of 0.92 V and fill factor of 45%. Following SVA, device efficiencies increase to 9.6%, largely retaining an open-circuit voltage of 0.90 V yet with a significantly improved fill factor of 72%, owing to the reduced bimolecular recombination (Figure 5c and 5d).

The EA kinetic trace normalized by the charge population gives the amount of EA per unit charge in the active layer (Figure 4d, right axis, Figure 5e, middle) where the EA signal increases for hundreds of picoseconds and saturates at the nanosecond time scale. We note that this time scale is at least 1 order of magnitude faster than the normally reported fastest carrier transit times, indicating that this effect would not necessarily result in poor carrier diffusion. The EA signal rise is also correlated with a red shift of the polaron signal maximum over time (Figure 3c). This indicates that the electric field builds as hole polarons migrate from intermixed higher energy regions and pool in lower energy BQR aggregates. This energetic cascade can provide a driving force to enable spatial separation of electrons and holes and has been shown to lead to longer lived populations of extractable charges.[40,41] Further evidence to support the importance of a morphological energetic cascade can be seen by measuring the transient spectra of a blend with a dilute acceptor component. We see the complete absence of the electroabsorption signal when acceptor molecules are isolated in the blend by examining a 95:5 BQR:PC$_{71}$BM SVA film (Figure S16). Excitons undergo charge separation to form polarons within this blend; however, we see no evidence of charge buildup or capacitive charging due to the absence of the cascade needed to form such a charge buildup.

The electric field buildup may be also caused by built-in nanoscale electrostatic effects within the active layer, fortifying the energetic cascade. The collective action of the anisotropic distribution of electronic density in typical aggregated conjugated molecules has been discussed widely in the theory and simulation of organic aggregates,[42−45] though it is difficult to measure experimentally, especially at buried interfaces. This effect has been calculated to significantly alter the energetic landscape for charge carriers in aggregate films.[44] While static microscopic electric fields caused only by molecular arrangement can cause built-in electric fields, this effect would cancel in a differential transient absorption measurement. However, a flow of migrating photoinduced charge carriers as directed by the potential energy landscape of built-in fields would be evident in an electroabsorption signal in such a pump-on, pump-off experiment.

In contrast to photoinduced absorption signals, which should scale linearly with film thickness, the electroabsorption signature exhibits a more significant thickness-dependent behavior in SVA films (Figure 4f, Figure 3e−g, and Figure S14). Charge carriers produce local electric fields, where the amount of ΔA signal originating from the Stark effect is proportional to the electric field squared, $\vec{E}^2$. Thicker films contain a greater number of photogenerated carriers, leading to a more significant scaling in the EA signal than a standard optical transition with increasing active layer thickness. We note that this phenomenon was only easily detectable in transient absorption measurements with relatively thick junctions. Consequently, it is possible that there are existing systems where this same effect may be present but could have remained undetected.

The charge migration and large electric field buildup observed here in the SVA heterojunction is analogous to the charging of a capacitor (Figure 5e). We emphasize that all transient experiments were undertaken on only the device active layer, equivalent to a device at V_{OC}. The addition of electrodes in a full device would provide an additional electric field aiding in the extraction of charges. Charges first stored away from the interface over nanosecond time scales can later be harvested at electrodes through drift and diffusion over the expected micro-millisecond time scales for carrier migration. We note that this result contrasts with the accepted idea of an ideal open-circuit device where radiative recombination should be at a maximum.[46] It shows that morphology can influence the fate of charges across interfaces for the first nanoseconds following photoexcitation, potentially suggesting a more nuanced way to understand charge migration and V_{OC} in organic photovoltaics. The presence of interdomain electric fields could allow for the existence of charge throughout the device, which would prevent the presence of space charge regions at contacts that limit fill factors.[47] The devices with SVA treatment are able to maintain good efficiencies in even thicker active layers than those studied here, up to 8.1% in a 600 nm active layer and a fill factor of 61% (Table S1). The relationship between efficient thick heterojunctions and the capacitive charging reported here is the topic of ongoing and future investigations.

Steady-state electroabsorption measurements (Figure S10a and S10b) were used to calibrate the observed Stark effect. The observed field at its maximum value is estimated at 487 kV/cm, extremely large compared to that expected locally between domains and unprecedented in photovoltaic systems. This value is somewhat comparable to fields generated from charges that are held in nanoscale proximity such as in ultracapacitors[48] and photogenerated ion pairs.[49] The relative dielectric constants of organic semiconductors are generally between 2 and 4, which is comparable to that of a dielectric layer in a standard macroscopic capacitor. Due to this dielectric environment, the electric fields responsible for the EA will polarize the intervening medium between regions of high charge density, causing charges to be further shielded from their mutual attraction at the interface. This suggests that in devices where charge separation can occur efficiently, the low dielectric constant (often cited as a hindrance in organic photovoltaics) could actually help carriers avoid bimolecular recombination.

CONCLUSIONS

Our results show that free charges can build up in crystalline domains in an organic bulk heterojunction film with large electric fields of up to ~487 kV/cm generated between positive and negative carriers. Rather than a decay of the electric field as charges separate over time, we see the opposite with a field increasing in magnitude up to 1 ns as a capacitive buildup occurs. Charges must be in close proximity to one another (<5 nm) in order to form and maintain such large electric fields. Surprisingly, spectroscopic, device, and charge recombination data show that charges are protected by this capacitive charging and recombination is substantially suppressed by up to 2000 times compared to the Langevin rate.

We show that charges are protected over the early time scales of carrier migration and that the resulting capacitive charging is not detrimental to the migration of charges as it is for traps and defects. These observations are particularly interesting given the debate regarding how photogenerated charge pairs escape and avoid the predicted strong Coulombic attraction between carriers in organic heterojunctions and how only some materials can support thick junctions.[7,50,51]

Given that the transient signature of these electric fields may be easily obscured in spectroscopic measurements—only appearing clearly in thicker active layers—we speculate that this phenomenon might be found in other material blends, especially those that support efficient thick devices and have suppressed recombination. Beyond simply the role of donor and acceptor components, we show that the local environment of interfaces and their energetic landscapes can make a key contribution to the fate of photogenerated charges within a photovoltaic system. The capacitor-like charge buildup we observe shows that nanomorphology and electric fields in photovoltaics can play an unexpected role in protecting photogenerated charges from recombination, thus suggesting a significant new design principle for optimizing OPV devices.

ASSOCIATED CONTENT

Supporting Information

The Supporting Information is available free of charge at https://pubs.acs.org/doi/10.1021/jacs.9b12526.

> Supplementary text, figures, and tables on device performance, bulk heterojunction morphology, transient absorption measurements, Stark effect in organic photovoltaic blends, transient absorption spectral extraction using a genetic algorithm, and triplet exciton generation in as-cast BQR blends, and references (PDF)

AUTHOR INFORMATION

Corresponding Authors

Gregory D. Scholes – *Department of Chemistry, Princeton University, Princeton, New Jersey 08544, United States; School of Chemistry, University of Melbourne, Parkville 3010, Australia;* orcid.org/0000-0003-3336-7960; Email: gscholes@princeton.edu

Kenneth P. Ghiggino – *School of Chemistry, University of Melbourne, Parkville 3010, Australia;* orcid.org/0000-0001-6621-4448; Email: ghiggino@unimelb.edu.au

Other Authors

Kyra N. Schwarz – *Department of Chemistry, Princeton University, Princeton, New Jersey 08544, United States; School of Chemistry, University of Melbourne, Parkville 3010, Australia*

Paul B. Geraghty – *Bio21 Institute and School of Chemistry, University of Melbourne, Parkville 3010, Australia*

Valerie D. Mitchell – *Bio21 Institute and School of Chemistry, University of Melbourne, Parkville 3010, Australia*

Saeed-Uz-Zaman Khan – *Department of Electrical Engineering, Princeton University, Princeton, New Jersey 08544, United States*

Oskar J. Sandberg – *Department of Physics, Swansea University, Swansea SA2 8PP, United Kingdom*

Nasim Zarrabi – *Department of Physics, Swansea University, Swansea SA2 8PP, United Kingdom*

Bryan Kudisch – *Department of Chemistry, Princeton University, Princeton, New Jersey 08544, United States*

Jegadesan Subbiah – *Bio21 Institute and School of Chemistry, University of Melbourne, Parkville 3010, Australia*

Trevor A. Smith – *School of Chemistry, University of Melbourne, Parkville 3010, Australia;* orcid.org/0000-0003-4453-9713

Barry P. Rand – *Department of Electrical Engineering and Andlinger Center for Energy and the Environment, Princeton University, Princeton, New Jersey 08544, United States;* orcid.org/0000-0003-4409-8751

Ardalan Armin – *Department of Physics, Swansea University, Swansea SA2 8PP, United Kingdom;* orcid.org/0000-0002-6129-5354

David J. Jones – *Bio21 Institute and School of Chemistry, University of Melbourne, Parkville 3010, Australia;* orcid.org/0000-0003-1088-7744

Complete contact information is available at:
https://pubs.acs.org/10.1021/jacs.9b12526

Notes

The authors declare no competing financial interest.

■ ACKNOWLEDGMENTS

K.N.S. would like to acknowledge Matthew Menke and Lee Richter for helpful discussions and Simone Gélinas for contributions to developing the genetic algorithm software. This work was made possible by support from the Australian Renewable Energy Agency, which funds the project grants within the Australian Centre for Advanced Photovoltaics. K.N.S acknowledges the Australian Renewable Energy Agency for a postgraduate scholarship. G.D.S and K.N.S. acknowledge support by the U.S. Department of Energy, Office of Science, Office of Basic Energy Sciences Solar Photochemistry program under Award Number DE-SC0015429. S.U.Z.K. and B.P.R. acknowledge funding from the U.S. Department of Energy, Office of Basic Energy Sciences, Division of Materials Sciences and Engineering under Award Number DE-SC0012458. A.A. is a Sêr Cymru II Rising Star Fellow supported by the European Regional Development Fund, Welsh European Funding Office, and Swansea University strategic initiative in Sustainable Advanced Materials. B.K. acknowledges support by the National Science Foundation Graduate Research Fellowship under Grant Number DGE-1656466.

■ REFERENCES

(1) Polman, A.; Knight, M.; Garnett, E. C.; Ehrler, B.; Sinke, W. C. Photovoltaic Materials: Present Efficiencies and Future Challenges. *Science* **2016**, *352* (6283), No. aad4424.

(2) Brédas, J.-L.; Norton, J. E.; Cornil, J.; Coropceanu, V. Molecular Understanding of Organic Solar Cells: The Challenges. *Acc. Chem. Res.* **2009**, *42* (11), 1691−1699.

(3) Blankenship, R. E. *Molecular Mechanisms of Photosynthesis*; Blackwell Science, 2002.

(4) Haugeneder, A.; Neges, M.; Kallinger, C.; Spirkl, W.; Lemmer, U.; Feldmann, J.; Scherf, U.; Harth, E.; Gugel, A.; Mullen, K. Exciton Diffusion and Dissociation in Conjugated Polymer/Fullerene Blends and Heterostructures. *Phys. Rev. B: Condens. Matter Mater. Phys.* **1999**, *59* (23), 15346−15351.

(5) Collins, S. D.; Ran, N. A.; Heiber, M. C.; Nguyen, T.-Q. Small Is Powerful: Recent Progress in Solution-Processed Small Molecule Solar Cells. *Adv. Energy Mater.* **2017**, *7* (10), 1602242.

(6) Lakhwani, G.; Rao, A.; Friend, R. H. Bimolecular Recombination in Organic Photovoltaics. *Annu. Rev. Phys. Chem.* **2014**, *65* (1), 557−581.

(7) Meredith, P.; Armin, A. Scaling of next Generation Solution Processed Organic and Perovskite Solar Cells. *Nat. Commun.* **2018**, *9* (1), 8−11.

(8) Armin, A.; Chen, Z.; Jin, Y.; Zhang, K.; Huang, F.; Shoaee, S. A Shockley-Type Polymer: Fullerene Solar Cell. *Adv. Energy Mater.* **2018**, *8* (7), 1701450.

(9) Armin, A.; Subbiah, J.; Stolterfoht, M.; Shoaee, S.; Xiao, Z.; Lu, S.; Jones, D. J.; Meredith, P. Reduced Recombination in High Efficiency Molecular Nematic Liquid Crystalline: Fullerene Solar Cells. *Adv. Energy Mater.* **2016**, *6* (22), 1600939.

(10) Jin, Y.; Chen, Z.; Xiao, M.; Peng, J.; Fan, B.; Ying, L.; Zhang, G.; Jiang, X.-F.; Yin, Q.; Liang, Z.; Huang, F.; Cao, Y. Thick Film Polymer Solar Cells Based on Naphtho[1,2-c:5,6-c]bis[1,2,5]thiadiazole Conjugated Polymers with Efficiency over 11%. *Adv. Energy Mater.* **2017**, *7* (22), 1700944.

(11) Langevin, M. Recombinaison et Diffusion Des Ions Gazeux. *J. Phys. Theor. Appl.* **1905**, *4* (1), 322−333.

(12) Bublitz, G.; Boxer, S. Stark Spectroscopy: Applications in Chemistry, Biology, and Materials Science. *Annu. Rev. Phys. Chem.* **1997**, *48*, 213−242.

(13) Boxer, S. Stark Realities. *J. Phys. Chem. B* **2009**, *113*, 2972−2983.

(14) Gulbinas, V.; Kananavičius, R.; Valkunas, L.; Bässler, H. Dynamic Stark Effect as a Probe of the Evolution of Geminate Electron-Hole Pairs in a Conjugated Polymer. *Phys. Rev. B: Condens. Matter Mater. Phys.* **2002**, *66* (23), 1−4.

(15) Cabanillas-Gonzalez, J.; Virgili, T.; Gambetta, A.; Lanzani, G.; Anthopoulos, T. D.; De Leeuw, D. M. Photoinduced Transient Stark Spectroscopy in Organic Semiconductors: A Method for Charge Mobility Determination in the Picosecond Regime. *Phys. Rev. Lett.* **2006**, *96* (10), 6−9.

(16) Klimov, V. I. Spectral and Dynamical Properties of Multiexcitons in Semiconductor Nanocrystals. *Annu. Rev. Phys. Chem.* **2007**, *58*, 635−673.

(17) Ardo, S.; Sun, Y.; Castellano, F. N.; Meyer, G. J. Excited-State Electron Transfer from Ruthenium-Polypyridyl Compounds to Anatase TiO_2 Nanocrystallites: Evidence for a Stark Effect. *J. Phys. Chem. B* **2010**, *114* (45), 14596−14604.

(18) Koch, M.; Myahkostupov, M.; Oblinsky, D. G.; Wang, S.; Garakyaraghi, S.; Castellano, F. N.; Scholes, G. D. Charge Localization after Ultrafast Photoexcitation of a Rigid Perylene Perylenediimide Dyad Visualized by Transient Stark Effect. *J. Am. Chem. Soc.* **2017**, *139* (15), 5530−5537.

(19) Scarongella, M.; De Jonghe-Risse, J.; Buchaca-Domingo, E.; Causa', M.; Fei, Z.; Heeney, M.; Moser, J.-E.; Stingelin, N.; Banerji, N. A Close Look at Charge Generation in Polymer: Fullerene Blends with Microstructure Control. *J. Am. Chem. Soc.* **2015**, *137* (8), 2908−2918.

(20) Gelinas, S.; Rao, A.; Kumar, A.; Smith, S. L.; Chin, A. W.; Clark, J.; van der Poll, T. S.; Bazan, G. C.; Friend, R. H. Ultrafast Long-Range Charge Separation in Organic Semiconductor Photovoltaic Diodes. *Science* **2014**, *343* (6170), 512−516.

(21) Menke, S. M.; Cheminal, A.; Conaghan, P.; Ran, N. A.; Greehnam, N. C.; Bazan, G. C.; Nguyen, T. Q.; Rao, A.; Friend, R. H. Order Enables Efficient Electron-Hole Separation at an Organic Heterojunction with a Small Energy Loss. *Nat. Commun.* **2018**, *9* (1), 1−7.

(22) Tamai, Y.; Fan, Y.; Kim, V. O.; Ziabrev, K.; Rao, A.; Barlow, S.; Marder, S. R.; Friend, R. H.; Menke, S. M. Ultrafast Long-Range Charge Separation in Nonfullerene Organic Solar Cells. *ACS Nano* **2017**, *11* (12), 12473−12481.

(23) Geraghty, P. B.; Lee, C.; Subbiah, J.; Wong, W. W. H.; Banal, J. L.; Jameel, M. A.; Smith, T. A.; Jones, D. J. High Performance P-Type Molecular Electron Donors for OPV Applications via Alkylthiophene Catenation Chromophore Extension. *Beilstein J. Org. Chem.* **2016**, *12*, 2298−2314.

(24) Sandberg, O. J.; Nyman, M.; Österbacka, R. Effect of Contacts in Organic Bulk Heterojunction Solar Cells. *Phys. Rev. Appl.* **2014**, *1* (2), 1−15.

(25) Pettersson, L. A. A.; Roman, L. S.; Inganäs, O. Modeling Photocurrent Action Spectra of Photovoltaic Devices Based on Organic Thin Films. *J. Appl. Phys.* **1999**, *86* (1), 487−496.

(26) Sugunan, S. K.; Robotham, B.; Sloan, R. P.; Szmytkowski, J.; Ghiggino, K. P.; Paige, M. F.; Steer, R. P. Photophysics of Untethered ZnTPP-Fullerene Complexes in Solution. *J. Phys. Chem. A* **2011**, *115* (44), 12217−12227.

(27) Stevens, M. A.; Silva, C.; Russell, D. M.; Friend, R. H. Exciton Dissociation Mechanisms in the Polymeric Semiconductors Poly(9,9-Dioctylfluorene) and Poly(9,9-Dioctylfluorene-Co-Benzothiadiazole). *Phys. Rev. B: Condens. Matter Mater. Phys.* **2001**, *63* (16), 165213.

(28) Ferguson, A. J.; Kopidakis, N.; Shaheen, S. E.; Rumbles, G. Quenching of Excitons by Holes in Poly(3-Hexylthiophene) Films. *J. Phys. Chem. C* **2008**, *112* (26), 9865−9871.

(29) Hodgkiss, J. M.; Albert-Seifried, S.; Rao, A.; Barker, A. J.; Campbell, A. R.; Marsh, R. A.; Friend, R. H. Exciton-Charge Annihilation in Organic Semiconductor Films. *Adv. Funct. Mater.* **2012**, *22* (8), 1567−1577.

(30) Frisch, M. J.; Trucks, G. W.; Schlegel, H. B.; Scuseria, G. E.; Robb, M. A.; Cheeseman, J. R.; Scalmani, G.; Barone, V.; Petersson, G. A.; Nakatsuji, H.; Li, X.; Caricato, M.; Marenich, A. V.; Bloino, J.; Janesko, B. G.; Gomperts, R.; Mennucci, B.; Hratchian, H. P.; Ortiz, J. V.; Izmaylov, A. F.; Sonnenberg, J. L.; Williams-Young, D.; Ding, F.; Lipparini, F.; Egidi, F.; Goings, J.; Peng, B.; Petrone, A.; Henderson, T.; Ranasinghe, D.; Zakrzewski, V. G.; Gao, J.; Rega, N.; Zheng, G.; Liang, W.; Hada, M.; Ehara, M.; Toyota, K.; Fukuda, R.; Hasegawa, J.; Ishida, M.; Nakajima, T.; Honda, Y.; Kitao, O.; Nakai, H.; Vreven, T.; Throssell, K.; Montgomery, J. A., Jr.; Peralta, J. E.; Ogliaro, F.; Bearpark, M. J.; Heyd, J. J.; Brothers, E. N.; Kudin, K. N.; Staroverov, V. N.; Keith, T. A.; Kobayashi, R.; Normand, J.; Raghavachari, K.; Rendell, A. P.; Burant, J. C.; Iyengar, S. S.; Tomasi, J.; Cossi, M.; Millam, J. M.; Klene, M.; Adamo, C.; Cammi, R.; Ochterski, J. W.; Martin, R. L.; Morokuma, K.; Farkas, O.; Foresman, J. B.; Fox, D. J. *Gaussian 16*; Gaussian, Inc.: Wallingford, CT, 2016.

(31) Heiber, M. C.; Nguyen, T. Q.; Deibel, C. Charge Carrier Concentration Dependence of Encounter-Limited Bimolecular Recombination in Phase-Separated Organic Semiconductor Blends. *Phys. Rev. B: Condens. Matter Mater. Phys.* **2016**, *93* (20), 1−8.

(32) Shoaee, S.; Armin, A.; Stolterfoht, M.; Hosseini, S. M.; Kurpiers, J.; Neher, D. Decoding Charge Recombination through Charge Generation in Organic Solar Cells. *Sol. RRL* **2019**, *3* (11), 1900184.

(33) Schwarz, K. N.; Geraghty, P. B.; Jones, D. J.; Smith, T. A.; Ghiggino, K. P. Suppressing Subnanosecond Bimolecular Charge Recombination in a High-Performance Organic Photovoltaic Material. *J. Phys. Chem. C* **2016**, *120* (42), 24002−24010.

(34) Rao, A.; Chow, P. C. Y.; Gélinas, S.; Schlenker, C. W.; Li, C.-Z.; Yip, H.-L.; Jen, A. K.-Y.; Ginger, D. S.; Friend, R. H. The Role of Spin in the Kinetic Control of Recombination in Organic Photovoltaics. *Nature* **2013**, *500* (7463), 435−439.

(35) Sajjad, M. T.; Zhang, Y.; Geraghty, P. B.; Mitchell, V. D.; Ruseckas, A.; Blaszczyk, O.; Jones, D. J.; Samuel, I. D. W. Tailoring Exciton Diffusion and Domain Size in Photovoltaic Small Molecules by Annealing. *J. Mater. Chem. C* **2019**, *7* (26), 7922−7928.

(36) Jakowetz, A. C.; Böhm, M. L.; Sadhanala, A.; Huettner, S.; Rao, A.; Friend, R. H. Visualizing Excitations at Buried Heterojunctions in Organic Semiconductor Blends. *Nat. Mater.* **2017**, *16* (5), 551−557.

(37) Vithanage, D. A.; Devižis, A.; Abramavičius, V.; Infahsaeng, Y.; Abramavičius, D.; MacKenzie, R. C. I.; Keivanidis, P. E.; Yartsev, A.; Hertel, D.; Nelson, J.; Sundström, V.; Gulbinas, V. Visualizing Charge Separation in Bulk Heterojunction Organic Solar Cells. *Nat. Commun.* **2013**, *4* (1), 2334.

(38) Gehrig, D. W.; Howard, I. A.; Laquai, F. F. Charge Carrier Generation Followed by Triplet State Formation, Annihilation, and Carrier Recreation in PBDTTT-C/PC 60 BM Photovoltaic Blends. *J. Phys. Chem. C* **2015**, *119* (24), 13509−13515.

(39) Jackson, N. E.; Savoie, B. M.; Marks, T. J.; Chen, L. X.; Ratner, M. A. The Next Breakthrough for Organic Photovoltaics? *J. Phys. Chem. Lett.* **2015**, *6* (1), 77−84.

(40) Vandewal, K.; Himmelberger, S.; Salleo, A. Structural Factors That Affect the Performance of Organic Bulk Heterojunction Solar Cells. *Macromolecules* **2013**, *46* (16), 6379−6387.

(41) Gallaher, J. K.; Prasad, S. K. K.; Uddin, M. A.; Kim, T.; Kim, J. Y.; Woo, H. Y.; Hodgkiss, J. M. Spectroscopically Tracking Charge Separation in Polymer:Fullerene Blends with a Three-Phase Morphology. *Energy Environ. Sci.* **2015**, *8* (9), 2713−2724.

(42) Heimel, G.; Salzmann, I.; Duhm, S.; Koch, N. Design of Organic Semiconductors from Molecular Electrostatics. *Chem. Mater.* **2011**, *23* (3), 359−377.

(43) D'Avino, G.; Muccioli, L.; Castet, F.; Poelking, C.; Andrienko, D.; Soos, Z. G.; Cornil, J.; Beljonne, D. Electrostatic Phenomena in Organic Semiconductors: Fundamentals and Implications for Photovoltaics. *J. Phys.: Condens. Matter* **2016**, *28* (43), 433002.

(44) Cornil, J.; Verlaak, S.; Martinelli, N.; Mityashin, A.; Olivier, Y.; Van Regemorter, T.; D'Avino, G.; Muccioli, L.; Zannoni, C.; Castet, F.; Beljonne, D.; Heremans, P. Exploring the Energy Landscape of the Charge Transport Levels in Organic Semiconductors at the Molecular Scale. *Acc. Chem. Res.* **2013**, *46* (2), 434−443.

(45) Tsiper, E. V.; Soos, Z. G. Charge Redistribution and Polarization Energy of Organic Molecular Crystals. *Phys. Rev. B: Condens. Matter Mater. Phys.* **2001**, *64* (19), 1−12.

(46) Miller, O. D.; Yablonovitch, E.; Kurtz, S. R. Strong Internal and External Luminescence as Solar Cells Approach the Shockley-Queisser Limit. *IEEE J. Photovoltaics* **2012**, *2* (3), 303−311.

(47) Tait, J. G.; Paetzold, U. W.; Cheyns, D.; Turbiez, M.; Heremans, P.; Rand, B. P. Interfacial Depletion Regions: Beyond the Space Charge Limit in Thick Bulk Heterojunctions. *ACS Appl. Mater. Interfaces* **2016**, *8* (3), 2211−2219.

(48) Stoller, M. D.; Park, S.; Zhu, Y.; An, J.; Ruoff, R. S. Graphene-Based Ultracapacitors. *Nano Lett.* **2008**, *8* (10), 3498−3502.

(49) Gosztola, D.; Yamada, H.; Wasielewski, M. R. Electric Field Effects of Photogenerated Ion Pairs on Nearby Molecules: A Model for the Carotenoid Band Shift in Photosynthesis. *J. Am. Chem. Soc.* **1995**, *117* (7), 2041−2048.

(50) Bakulin, A.; Rao, A.; Pavelyev, V. G.; van Loosdrecht, P. H. M.; Pshenichnikov, M. S.; Niedzialek, D.; Cornil, J.; Beljonne, D.; Friend, R. H. The Role of Driving Energy and Delocalized States for Charge Separation in Organic Semiconductors. *Science* **2012**, *335* (6074), 1340−1344.

(51) Vandewal, K.; Albrecht, S.; Hoke, E. T.; Graham, K. R.; Widmer, J.; Douglas, J. D.; Schubert, M.; Mateker, W. R.; Bloking, J. T.; Burkhard, G. F.; Sellinger, A.; Fréchet, J. M. J.; Amassian, A.; Riede, M. K.; McGehee, M. D.; Neher, D.; Salleo, A. Efficient Charge Generation by Relaxed Charge-Transfer States at Organic Interfaces. *Nat. Mater.* **2014**, *13* (1), 63−68.